Journal of Materials Chemistry A

ROYAL SOCIETY OF CHEMISTRY

PAPER

View Article Online
View Journal

Cite this: DOI: 10.1039/d5ta06789h

Amphiphilic silane-MXene hybrids for high-performance flexible symmetric supercapacitors *via* additive-free processing

Thu Thuy Duong, [a] Se Huyn Kim *[b] and Juyoung Kim *[a]

Flexible and wearable microsupercapacitors demand MXene electrodes with strong substrate adhesion, high conductivity, and long-term mechanical durability—yet conventional MXene inks, relying on polymeric binders, suffer from conductivity loss and delamination due to weak interfacial interactions. A next-generation MXene ($Ti_3C_2T_x$) ink is developed, offering a transformative approach to flexible and wearable microsupercapacitors. Conventional MXene inks rely on polymeric binders to adhere to plastic substrates, but these binders typically degrade electrical conductivity and cause delamination due to weak interfacial interactions. Herein, a new class of MXene ink is formulated using a multifunctional alkoxysilane-based amphiphilic oligomer (AFAO) that acts simultaneously as a dispersant, an adhesion promoter, and a binder. This design enables MXene to be stably dispersed in organic solvents, strong adhesion to PET substrates, and retention of the intrinsic capacitance without any conductive additives. Electrodes prepared from this ink achieve 92.0% capacitance retention (211.2 F g^{-1} at 1 A g^{-1} in 1 M H_2SO_4) and maintain 100% performance after 1500 cycles under 180° bending. This multifunctional-ink strategy represents a significant paradigm shift in MXene processing, overcoming long-standing limitations in adhesion, dispersion stability, and electrochemical performance for flexible supercapacitor applications.

Received 21st August 2025
Accepted 17th September 2025

DOI: 10.1039/d5ta06789h

rsc.li/materials-a

1. Introduction

Titanium carbide MXene ($Ti_3C_2T_x$, where T_x = –O, –OH, halogens, or chalcogens) has attracted increasing attention in recent years owing to its unique two-dimensional morphology, rich surface chemistry, and outstanding physicochemical properties.[1–5] The abundant surface terminations allow MXenes to be applied in many fields, such as biomedicine, environmental remediation, and especially energy storage.[6–9] Among these applications, flexible energy storage devices are gaining significant attention, largely driven by the rapid development of intelligent wearable electronics.[10–13] This trend has created the need for a system that can be seamlessly integrated into compact devices or directly embedded into wearable platforms. Owing to their fast charge–discharge capability, lightweight nature, adaptability to various surface geometries, and compatibility with a wide range of bendable electronic components, flexible supercapacitors are considered ideal candidates for such applications. However, maintaining electrochemical performance under mechanical deformation is a critical requirement for flexible supercapacitors, making the fabrication of active material layers on flexible substrates such as PET a key technological challenge. These include not only the need for strong adhesion with plastic substrates and mechanical compliance under repeated bending and stretching, but also the requirement to achieve these without increasing the overall mass or dimensions of the device.

When flexible supercapacitor electrodes are fabricated from MXenes, the prevailing route involves printing an ink dispersion of MXene nanoflakes onto a plastic film substrate. Uniform deposition, followed by drying, inevitably requires a binder to secure the printed layer to the polymeric support. Conventional binders, such as poly(vinylidene fluoride) (PVDF), sodium carboxymethyl-cellulose (CMC-Na), and polytetrafluoroethylene (PTFE)—exhibit weak intermolecular interactions not only with MXene sheets but also with the plastic film.[14–18] Consequently, the printed electrodes tend to delaminate under bending, and, more critically, the insulating nature of these polymers severely degrades the intrinsic electrical conductivity and surface functionality of the MXene. Carbon-based conductive additives (*e.g.*, carbon black) are frequently introduced to offset this conductivity loss; however, such fillers readily agglomerate, create electrically inactive domains, and ultimately diminish overall energy-storage performance.[19–23] Because the use of a binder cannot be avoided for MXene patterning on flexible films, there is an urgent need for a next-

[a]*Nanocomposite Structure Polymer Lab, Department of Advanced Materials Engineering, Kangwon National University, Samcheok 25913, Republic of Korea. E-mail: juyoungk@kangwon.ac.kr*

[b]*School of Chemical Engineering, Konkuk University, Seoul 05029, Republic of Korea. E-mail: shkim97@konkuk.ac.k*

generation organic binder that preserves the conductivity of MXenes without auxiliary conductive fillers while simultaneously providing robust adhesion to the plastic substrate even under mechanical deformation.[20,24,25]

In this study, we propose an alkoxysilane-functionalized amphiphilic oligomer (AFAO) as a novel multifunctional binder for the MXene-based ink formulation. The AFAO not only serves as a binder that promotes strong interfacial adhesion to plastic substrates but also acts as a dispersing agent that stabilizes the MXene nanosheets in the solvent. This precursor consists of a polyethylene oxide (PEO)-based hydrophilic segment and a polypropylene oxide (PPO)-based hydrophobic segment containing reactive alkoxysilane groups. In our previous research, this precursor successfully played multiple roles: modulating the high reactivity of titanium tetraisopropoxide, acting as a nanodispersant for TiO_2 nanoparticles formed *via* a sol–gel reaction, and enabling the formation of a uniform, well-adhered dielectric hybrid coating layer on plastic substrates with nano-dispersed TiO_2.[26,27] Based on these results, we turned our attention to titanium carbide MXene, a two-dimensional material composed of titanium and carbon atoms arranged in a layered structure. MXene shares specific surface chemical characteristics with TiO_2, particularly the presence of hydroxyl and oxygen-containing groups, suggesting the potential compatibility of this compound. Motivated by these similarities, we extended the application of this amphiphilic oligomer to produce a multifunctional binder for MXene ink intended for the fabrication of flexible electrodes of SSCs, to achieve several objectives simultaneously, including (1) enhancing the adhesion between the MXene layer and plastic substrates; (2) providing steric stabilization within the ink *via* surface modification with the AFAO; (3) preventing flake restacking by increasing interlayer between MXene flakes; (4) simplifying the ink formulation with minimized additive required. Electrochemical measurements of the electrodes and SSC made from AFAO-modified MXene revealed that their specific capacitance was preserved without conductive fillers, along with enhanced resistance to mechanical deformation. This strategy presented a promising route toward MXene-based conductive inks that simultaneously meet the requirements for adhesion, dispersion stability, and electrochemical performance.

2. Results and discussion

2.1. Fabrication and characterization of AFAO-MXene

Fig. 1a schematically illustrates the fabrication procedure of AFAO-MXene ink. Detailed preparation steps are described in the Experimental section. Briefly, MXene multiflakes were synthesized by selectively etching the Al layers from the Ti_3AlC_2 MAX phase using HCl/LiF solution. The resulting etched material was dispersed in deionized water with sonication to obtain single- or few-layered MXene flakes, followed by solvent exchange with DMSO. To achieve a uniform distribution on the MXene surface, the AFAO was gradually added to the MXene dispersion and stirred for 6 hours prior to the addition of the catalyst. After completion of the reaction, the modified MXene was thoroughly washed several times to remove the unreacted AFAO and subsequently redispersed in DMSO. The resulting AFAO-MXene ink exhibited homogeneous and good dispersion

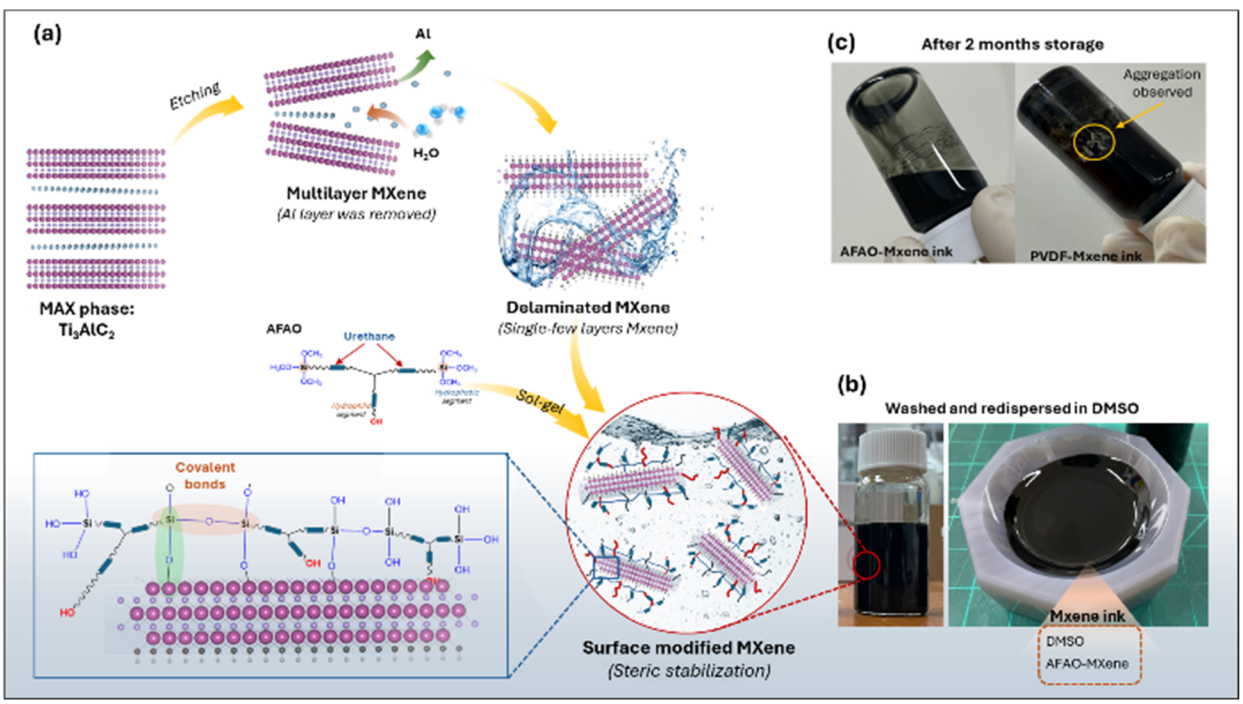

Fig. 1 (a) Schematic illustration of the surface modification process. (b) Optical images of AFAO-MXene ink. (c) Optical images of AFAO-MXene ink and PVDF-MXene ink stored for 2 months.

stability, as shown in Fig. 1b. After two months of storage, the AFAO-MXene ink demonstrated superior long-term stability, maintaining uniform dispersion (Fig. 1c and Video S1) whereas the PVDF-MXene ink became increasingly dense and exhibited severe agglomeration over time, forming a sludge-like texture. This enhanced stability in DMSO can be attributed to the successful formation of covalent bonds between the AFAO and the MXene surface, which provides steric stabilization in the solvent and effectively prevents the aggregation of MXene nanosheets over time. As illustrated in Fig. 1a, AFAO molecules chemically bond to the surface of MXene nanosheets *via* hydrolysis–condensation reactions between the alkoxysilane groups of the AFAO and the –OH groups on the MXene surface. Initially, the ethoxy groups ($-OC_2H_5$) of the AFAO undergo hydrolysis in the presence of water, forming silanol groups (Si–OH). These silanol groups subsequently undergo either self-condensation or react with surface hydroxyl groups on MXene, forming Si–O–Si or Ti–O–Si linkages which provide steric stabilization and prevent the aggregation of MXene flakes. The AFAO molecules, which are chemically grafted onto the surface of MXene through surface modification, contain urethane groups and ethylene oxide (EO) and propylene oxide (PO) segments. Each of these components is capable of forming hydrogen bonds with the carbonyl and hydroxyl groups present on the PET substrate. These interactions are anticipated to significantly enhance the interfacial adhesion between the MXene nanoflakes and the PET substrate. We will discuss the contribution of these chemically introduced AFAO functionalities to improved adhesion in relation to the bending test results of the SSC in a later section.

The morphology and microstructure of pristine MXene and AFAO-MXene samples were characterized by transmission electron microscopy (TEM) and scanning electron microscopy (SEM), as shown in Fig. 2. After selective etching of the Al layer from the MAX phase (Fig. S2, SI), multilayered MXene with a characteristic accordion-like morphology and well-defined interlayer spacing was obtained (Fig. 2a). Subsequent centrifugal separation yielded ultrathin, single-layered MXene nanosheets, which appeared thin, transparent, and flexible with a typical two-dimensional morphology, as shown in Fig. 2b and c. Fig. 2d shows the cross-sectional SEM image of AFAO-MXene nanosheets stacked on a vacuum-assisted filtration membrane, indicating that the nanosheets retained their monolayer morphology after surface modification. The SEM and TEM images of AFAO-MXene nanosheets (Fig. 2e and f) further confirmed that the layered structure of MXene was maintained after surface modification.

Fig. 3a presents the X-ray diffraction (XRD) patterns of various MXene samples. The disappearance of the characteristic peak of the MAX phase, typically observed at around 39° (2θ) and associated with the Al-layer, indicates the successful etching of the Al element and the subsequent formation of MXene. This is further confirmed using the Raman spectra as shown in Fig. 3b. The Raman spectrum of Ti_3AlC_2 shows characteristic bands at 193 and 265 cm^{-1}, corresponding to Al vibrations, and at 588 and 644 cm^{-1}, related to C vibrations. After etching, a new peak appears at 149 cm^{-1}, typical of $Ti_3C_2T_x$, while the disappearance of the 265 cm^{-1} peak confirms the removal of the Al layer. The C-related bands downshift to 569 and 615 cm^{-1}, and an additional peak at 393 cm^{-1} is attributed to O vibrations in the MXene sample. Moreover, strong peaks at 1400 and 1564 cm^{-1}, assigned to the D and G bands of graphitic carbon, become more intense after etching, indicating greater carbon exposure on the surfaces. The (002) peak in the XRD pattern also provides important information regarding the enlarged interlayer spacing and the altered crystallinity of MXene after modification with the AFAO. In contrast to the MAX phase, which displays a sharp and narrow (002) peak at a higher angle, all etched and exfoliated MXene samples exhibit a pronounced shift of the (002) peak toward lower angles, along with notable peak broadening. This shift is attributed to an increase in interlayer spacing, resulting from the removal of Al layers and the incorporation of surface terminations and structural disorder introduced during the exfoliation process.[28,29] Although the (002) peak of the PVDF-MXene sample also becomes broader, the interlayer *d*-spacing

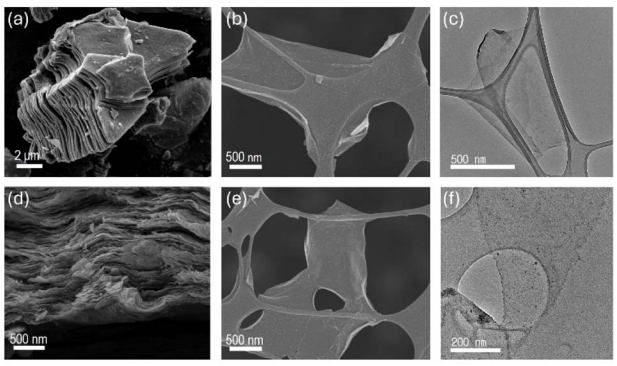

Fig. 2 SEM images of (a) multilayer pristine MXene and (b) single flake pristine MXene. (c) TEM image of single flake pristine MXene. (d) Cross-sectional SEM image of the AFAO-MXene film. (e) SEM images of single flake AFAO-MXene. (f) TEM image of single flake AFAO-MXene.

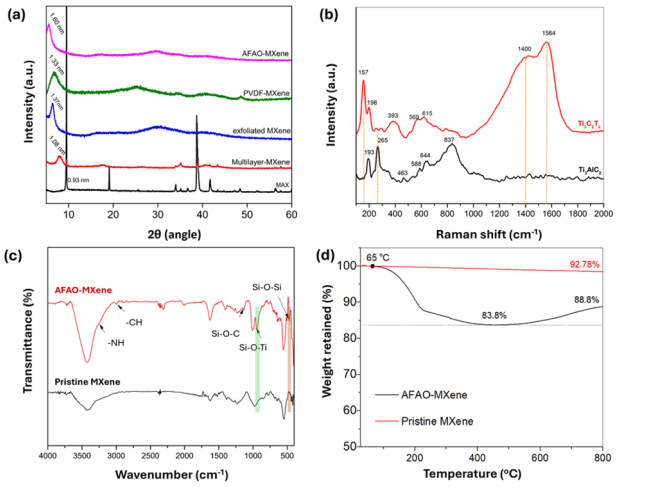

Fig. 3 (a) XRD patterns, (b) Raman spectra, (c) FTIR spectra, and (d) TGA curve of dried pristine MXene and AFAO-MXene.

remains nearly unchanged compared to the exfoliated MXene, suggesting that PVDF does not significantly intercalate between the MXene layers. Instead, it likely induces stacking disorder due to surface interactions or partial exfoliation, leading to reduced structural coherence along the *c*-axis. In contrast, pronounced weakening and further shift of the (002) peak to lower angles is observed in the AFAO-MXene sample. This behavior indicates that the MXene layers are arranged with low crystallographic order, exhibit increased interlayer expansion, and appear to adopt an amorphous-like morphology or exist as few-layer to single-layer structures. Based on the Bragg equation, the interlayer *d*-spacing between MXene flakes increased by 2.3 Å, from 13.7 Å to 16.0 Å, after surface modification with the AFAO. The XRD results reveal that the AFAO further increases the interlayer space compared with the pristine MXene and PVDF-MXene. This phenomenon can be attributed to the fact that the AFAO, with a lower molecular weight than PVDF, can move more flexibly and readily intercalate between MXene flakes. Upon successfully approaching the MXene surface, the AFAO forms covalent bonds *via* the sol–gel reaction, as previously illustrated in Fig. 1a. This surface anchoring effectively prevented the restacking of MXene nanosheets and contributed to an increased interlayer distance.

Fig. 3c represents the FTIR spectra of pristine MXene (black) and AFAO-MXenes (red) samples. For the pristine MXene sample, the characteristic peak at 549.6 cm^{-1} was most likely induced by the Ti–O bond deformation vibration or Ti–C bond vibrations on the surface.[30,31] Strong absorption bands observed at 3419.1 cm^{-1} and 1618.2 cm^{-1} are attributed to the stretching and bending vibrations of –OH groups, originating from both surface hydroxyls and adsorbed water molecules.[32–35] Meanwhile, the AFAO-MXene sample exhibited several new absorption bands, including a peak at 3263.8 cm^{-1} located to the right of the broad –OH band assigned to N–H stretching.[36] Additional peaks in the range of 2845.4–3023.6 cm^{-1} correspond to the stretching and deformation vibrations of C–H bonds. Furthermore, the appearance of a peak at 948 cm^{-1} is associated with Ti–O–Si bonding, while the peak at 470.1 cm^{-1} is attributed to Si–O–Si vibrations.[37–42]

The thermogravimetric (TGA) curve of MXene (Fig. 3d) reveals a slow degradation process due to the evaporation of physically absorbed moisture and the removal of the –OH and –F groups on the surface of the MXene, reaching a final weight loss rate of 7.22%. In contrast, AFAO-MXene shows a significant weight loss starting from approximately 65 °C to 225 °C, which corresponds closely to the surface modification reaction temperature and the degradation temperature of the AFAO. The weight continues to decrease to 83.8% at 420–500 °C (16.2% total mass loss), indicating that the majority of this loss is attributed to the organic layer grafted onto the MXene surface. At temperatures above 500 °C, carbonization is believed to occur as the carbon comes into contact with air. This also indicates that most of the AFAO molecules were effectively grafted to the surface of MXene.

The surface chemistry of MXene and AFAO-MXene was further characterized by X-ray photoelectron spectroscopy (XPS), and their chemical states were obtained using

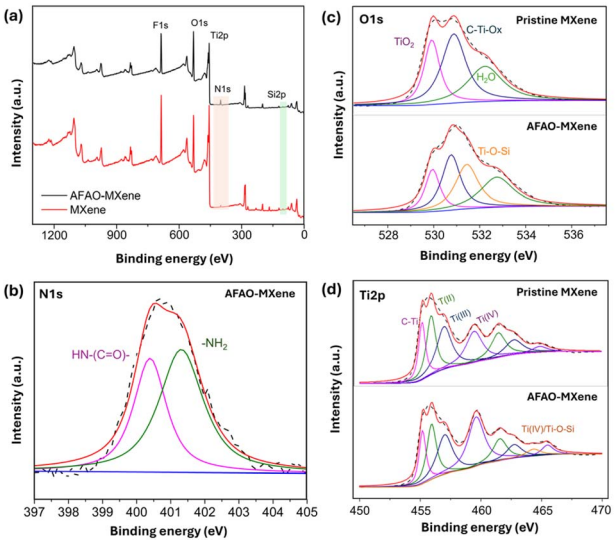

Fig. 4 XPS wide scan spectra of MXene before and after modification with the AFAO (a), high-resolution N 1s XPS spectra of AFAO-MXene (b), and O 1s (c) and Ti 2p XPS spectra (d) of pristine MXene and AFAO-MXene.

XPSPEAK41.[43] As illustrated in Fig. 4a, compared to pristine MXene, the lower intensity of the peaks related to F 1s and the corresponding higher N and O content can be found in AFAO-MXene. To confirm the presence of the AFAO on the MXene surface, the high resolution N 1s XPS spectrum was obtained (Fig. 4b). The spectrum was deconvoluted into two peaks corresponding to free amine and amide groups at binding energies of 401.4 and 400.4 eV, respectively. The deconvoluted O 1s spectra of pristine MXene and AFAO-MXene shown in Fig. 4c were deconvoluted into several sub-peaks: Ti–O–Ti bonds at 529.9 eV and hydroxyl groups associated with titanium (C–Ti–$(OH)_x$) appearing at around 531.6–532.7 eV.[44] In addition, a signal at approximately 530 eV was observed, indicating the presence of oxygen in a mixed oxide–fluoride environment ($TiO_{2-x}F_x$), which suggests partial substitution of oxygen by fluorine within the lattice.[44] Notably, no peak corresponding to Ti–O–Si asymmetric stretching was detected in pristine MXene, whereas a distinct peak was observed clearly in the AFAO-MXene sample at 531.5 eV in the O 1s spectrum.[37,45,46] This peak accounted for a substantial relative area of 28.3% compared to other surface oxygen species, confirming the successful formation of Ti–O–Si bonds following surface modification, which was consistent with the results of FT-IR (Table S1, SI). In Fig. 4d, the deconvoluted Ti 2p spectra revealed the presence of Ti–C, Ti(II), Ti(III), and Ti(IV) peaks corresponding to both Ti $2p_{3/2}$ and Ti $2p_{1/2}$ spin–orbit components in pristine MXene and AFAO-MXene.[47–49] In the pure MXene sample, the Ti(II) and Ti(III) peaks represent the unsaturated oxidation states of terminal titanium atoms within the MXene structure. After surface modification, another Ti(IV) peak at 464.4 eV was observed. This change can be attributed to the formation of Ti–O–Si bonds between MXene and the AFAO,

which is further confirmed using the O 1s XPS spectrum of the AFAO-MXene sample.

2.2. Electrochemical characterization of MXene electrodes

The AFAO-MXene ink was preliminarily tested for adhesion on PET substrates before being used to fabricate electrodes with fixed interfacial configurations (as shown in Video S2, SI). In addition, the zeta potential information of MXene before and after surface modification with the AFAO, shown in Fig. S3 (SI), indicates that after modification, MXene maintains a stable state in solution owing to steric stabilization. The wettability of the three types of inks on PET substrates was evaluated through

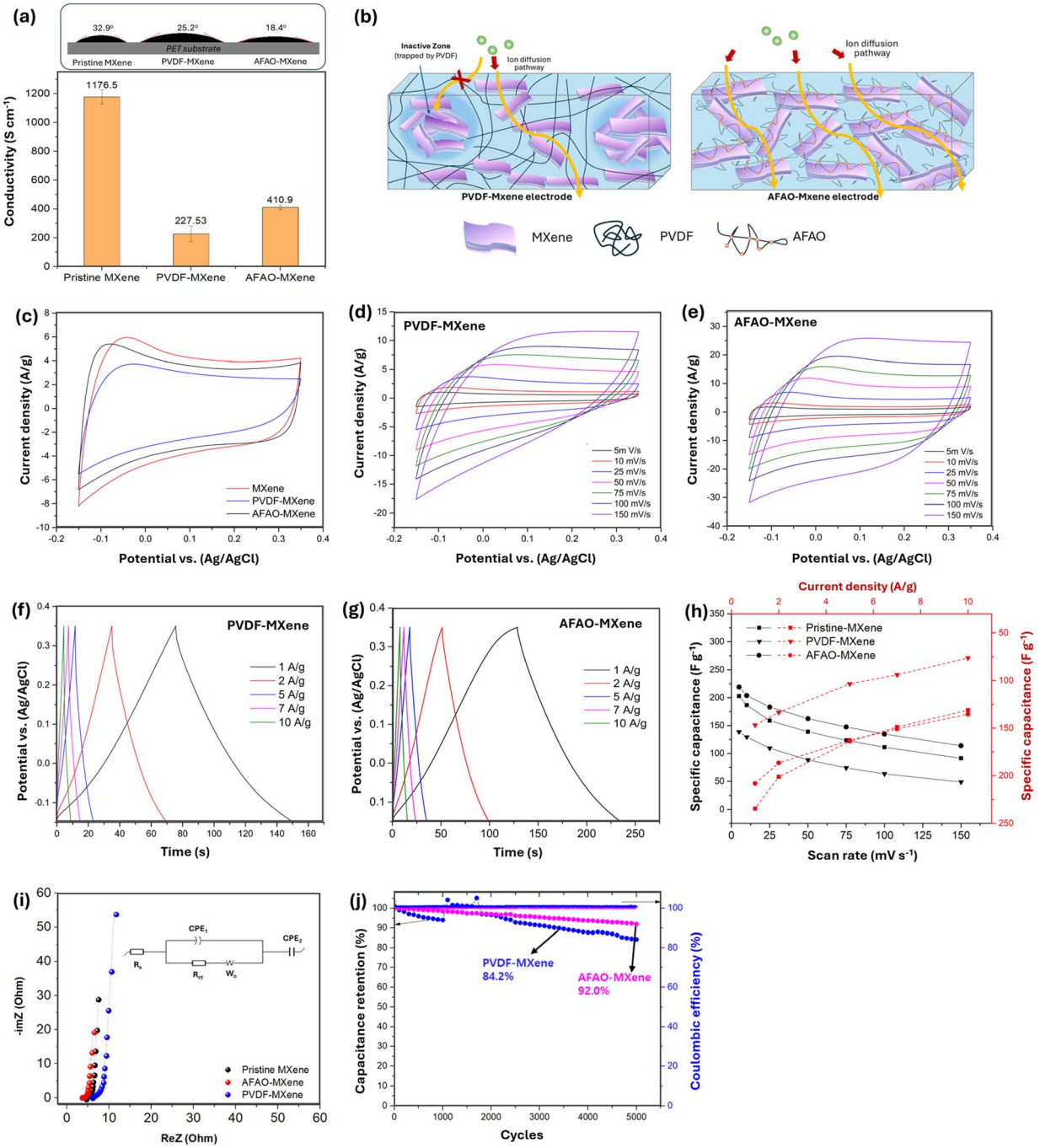

Fig. 5 Electrochemical performance of pristine MXene, PVDF and AFAO-MXene electrodes. (a) Contact angle of MXene ink on a PET substrate and conductivity (VAF films). (b) Ion diffusion in PVDF-MXene and AFAO-MXene electrodes. (c) CV curves of MXene, PVDF, and AFAO-MXene electrodes at a scan rate of 25 mV s^{-1}. (d and e) CV curves of PVDF-MXene and AFAO-MXene electrodes at 5–150 mV s^{-1}. (f and g) GCD curves of PVDF-MXene and AFAO-MXene electrodes at different current densities of 1.0–10 A g^{-1}. (h) The plot of specific capacitances of pristine MXene, PVDF-MXene and AFAO-MXene as a function of scan rate and current density. (i) Nyquist plot of pristine MXene, PVDF-MXene and AFAO-MXene in 1 M H_2SO_4; the inset shows a partially enlarged view of the high frequency region. (j) Cycling testing and coulombic efficiency of AFAO-MXene at 10 A g^{-1}.

contact angle measurements (Fig. 5a). After mixing MXene with PVDF or surface modifying with the AFAO, the inks exhibited improved wettability on PET, as indicated by the progressively decreasing contact angles: 32.9°, 25.2°, and 18.4° for pristine MXene ink, PVDF-MXene ink, and AFAO-MXene ink, respectively. Additionally, the electrical conductivity of vacuum-assisted filtration films prepared from the three inks was measured. The corresponding conductivity values were 1176.5 $\pm$ 34.5 S cm^{-1} for pristine MXene, 227.5 $\pm$ 50.1 S cm^{-1} for PVDF-MXene, and 410.9 $\pm$ 17.1 S cm^{-1} for AFAO-MXene. The PVDF-MXene ink exhibited a conductivity drop of 88.6%, while AFAO-MXene showed a reduction of 65.1%. This conductivity difference may partially explain the variations in electrochemical performance discussed below.

The electrochemical properties of the MXene electrodes were evaluated using a standard three-electrode system in 1 M H_2SO_4 electrolyte. After optimization across various voltage ranges with the results shown in Fig. S4 (SI), a potential window of -0.15 to 0.35 V was selected. Under the same CV scan conditions, the area enclosed by the CV curve is proportional to the specific capacitance of the electrode. Fig. 5c shows the results of CV tests of the three kinds of electrodes, all of which exhibit a relatively rectangular-shaped CV profile over the operating potential window, indicating that the primary charge storage mechanism is based on the electrochemical double layer. Among these electrodes, the PVDF-MXene electrode shows the smallest CV area, corresponding to the lowest charge storage capacity compared to the pristine MXene electrode and AFAO-MXene electrode. Fig. 5d and e separately show the CV curves at different scan rates from 5 mV s^{-1} to 150 mV s^{-1} of PVDF-MXene and AFAO-MXene electrodes. Fig. 5g shows the relationship between gravimetric specific capacitance and the scan rate (black) and current density (red) based on the CV and GCD curves. The maximum gravimetric specific capacitances of the pure MXene, PVDF-MXene, and AFAO-MXene electrodes, achieved at a low scan rate of 5 mV s^{-1}, were 202.7 F g^{-1}, 138.8 F g^{-1} and 219.1 F g^{-1}, respectively. At a low current density of 1 A g^{-1}, the corresponding values were 234.5 F g^{-1}, 146.9 F g^{-1}, and 208.3 F g^{-1}, respectively. At the start of a discharge curve, a slight variation in potential can be observed which is due to the sudden drop in current at the start of the discharge due to the internal resistance (IR) drop present at every half-cycle. This IR drop will reduce the power and capacity of the material under test. To explain the regions clearly, the charge/discharge curve at 1 A g^{-1} is plotted separately in Fig. S5 (SI). These results indicate that the AFAO-MXene sample is capable of maintaining its electrochemical performance. The surface modification of MXene appears not to hinder charge transport pathways. In contrast, the insulating nature and large molecular size of PVDF in PVDF-MXene electrodes may block ion diffusion pathways and occupy active charge storage sites, resulting in undesired inactive MXene zones (as illustrated in Fig. 5b). In these zones, electrolytes have limited access to the MXene surface, thereby hindering ion transport and reducing the number of accessible charge storage sites. As a result, the overall charge storage capacity is diminished. The EIS measurements presented in the following section will further clarify the underlying ion transport and charge storage mechanisms.

Fig. 5i shows the Nyquist plots of the three types of electrodes measured under open-circuit conditions over a frequency range of 0.01 to 10^5 Hz. The data were fitted using a five-component equivalent circuit. In these plots, the high-frequency interception on the real axis corresponds to the solution resistance (R_s), while the semicircle in the mid-frequency region represents the charge transfer resistance (R_{ct}). Lower R_{ct} values suggest faster ion transport, as summarized in Table S2 (SI). R_{ct} values for pristine MXene, PVDF-MXene, and AFAO-MXene were 1.657 Ω, 3.149 Ω, and 0.673 Ω, respectively. The increased R_{ct} observed in the PVDF-MXene sample may be attributed to the use of the PVDF binder in the absence of conductive additives that hindered charge transport between MXene layers, thereby indirectly reducing the overall charge storage performance. Additionally, the fitted circuit model revealed a notable increase in the Warburg coefficient (σ) for the PVDF-MXene sample, reaching 1.963 compared to 1.339 for pristine MXene. In contrast, the σ value slightly decreased to 1.202 in the AFAO-MXene sample. In the low-frequency region, PVDF-MXene Nyquist plots showed a lower slope compared to the near-vertical line of AFAO-MXene, indicating impeded ion diffusion into charge storage sites and a consequent reduction in capacitance. This suggests that ion diffusion in PVDF-MXene is more hindered, possibly due to blocked pathways or reduced electrolyte accessibility, whereas modification of MXene with the AFAO can improve ion transport by maintaining open diffusion channels (as shown in Fig. 5b).

The cycling stability of PVDF-MXene and AFAO-MXene electrodes is assessed through repeated charge–discharge recordings at a substantial current density of 10 A g^{-1} over 5000 consecutive cycles as depicted in Fig. 5j. The capacitance retention of both electrode samples demonstrates relatively high stability, with values of 82.2% and 91.2% for PVDF-MXene and AFAO-MXene electrodes, respectively. In addition, it is noteworthy that the coulombic efficiency remains consistently around 100%, indicating that both electrodes exhibit excellent coulombic efficiency signifying their extraordinary cycling stability and reversibility.

2.3. Electrochemical characterization and the bending test of SSCs

Two types of SSC were fabricated using PVDF-MXene and AFAO-MXene electrodes. These electrodes were cast onto PET substrates with an active area of 2 cm^2 and a uniform mass loading of 1 mg cm^{-2} using PVA/H_2SO_4 gel as the solid-state electrolyte, following the preparation procedure illustrated in Fig. 6a. According to the two-electrode test results and CV scans over a voltage range of 0.6–1.2 V, the operating window of the flexible all-solid-state SSC was set to 0–1.0 V (Fig. S4d, SI). The results of CV measurements performed for both the PVDF-SSC and AFAO-SSC are shown in Fig. 6b and c. The CV curves at various scan rates up to 150 mV s^{-1} are presented in Fig. S6 (SI). A quick comparison of the CV scanning results of these SSCs

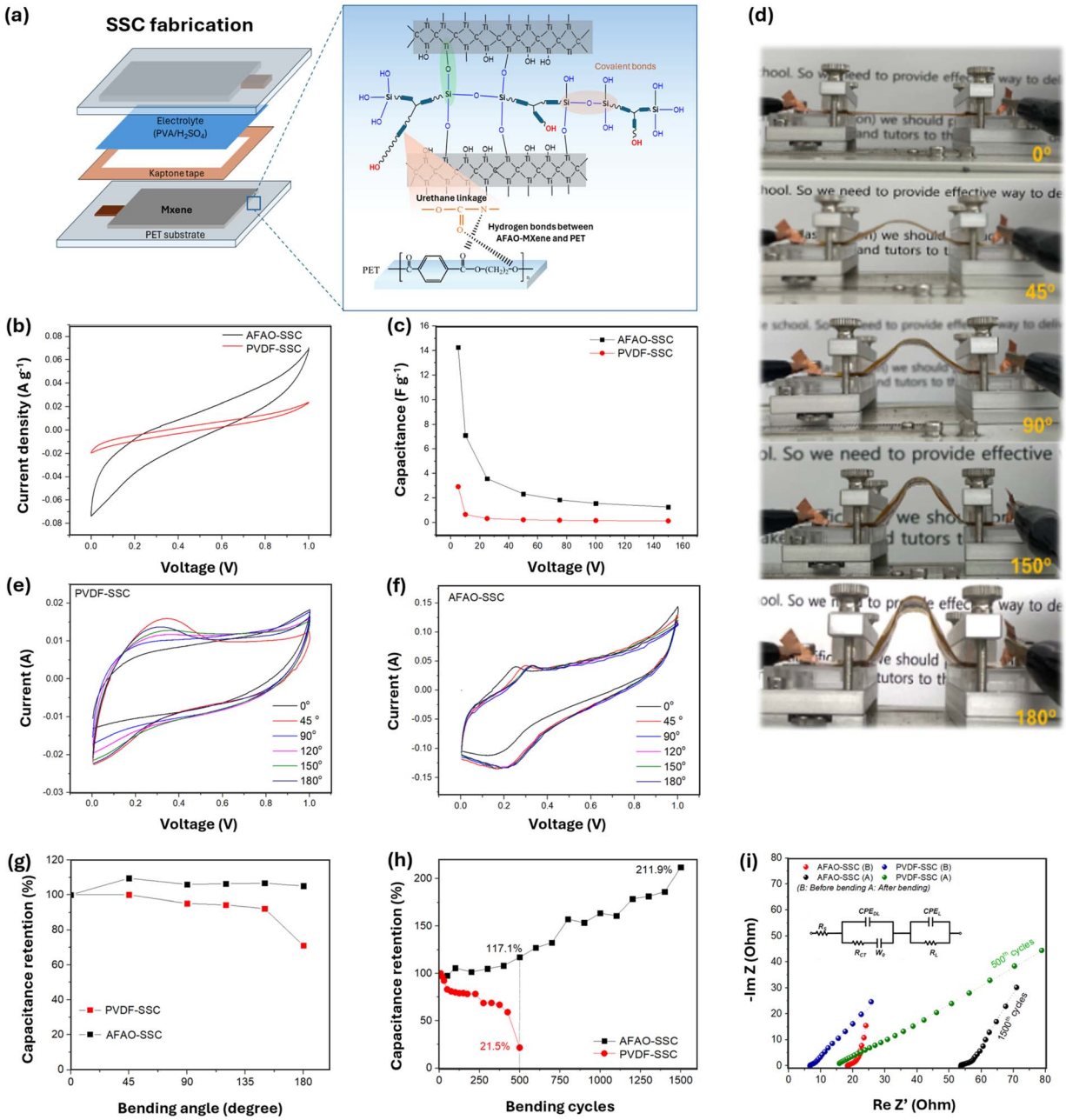

Fig. 6 (a) SSC fabrication and optical image of the MXene SSC and the mechanism of enhancing adhesion between AFAO-MXene and the PET substrate. (b) CV curves of the PVDF-SSC and AFAO-SSC at 5 mV s^{-1}. (c) CV curves of the PVDF-SSC and AFAO-SSC at different scan rates. (d and e) CV curves of the PVDF-SSC and AFAO-SSC at different banding angles (25 mV s^{-1}). (f) Optical image of the bending system for the bending test. (g) Capacitance retention after bending at different angles of the PVDF-SSC and AFAO-SSC. (h) Bending stability test of PVDF-SSC and AFAO-SSC at 180° bending. (i) Nyquist plot of the PVDF-SSC and AFAO-SSC before and after the bending stability test.

shows that the AFAO-SSC clearly exhibits a much larger enclosed area than the PVDF-SSC, indicating superior charge storage capability. Both devices achieved their highest capacitance at a scan rate of 5 mV s^{-1}, with the AFAO-SSC reaching a specific capacitance of 14.3 F g^{-1} that is nearly five times higher than that of the PVDF-SSC (2.92 F g^{-1}). These electrochemical behaviors are consistent with the observations in the previous three-electrode tests, where the decline in specific capacitance and the significant loss of electrical conductivity in the electrode made from PVDF-MXene ink ultimately led to a reduction in the overall charge storage capacity of the supercapacitor.

In practical applications such as wearable electronics, devices are often subjected to repeated mechanical deformation due to human activities. Therefore, evaluating the electrochemical stability and mechanical durability of flexible energy

storage systems under such conditions is important especially when integrating with flexible substrates like PET. This evaluation shows whether the device remains stable over time and also provides insight into how strongly the electrode material adheres to the substrate. In this study, the bending tests were carried out at various bending angles and across different numbers of bending cycles to assess both the retention of electrochemical performance and, indirectly, the adhesion stability of the MXene electrode layer after surface modification with the AFAO. The bending test was carried out using a linear movement mechanism with one end fixed and the other moving horizontally, as illustrated in Fig. 6d, and experimental details are presented in Video S3 (SI). CV measurements at a scan rate of 25 mV s^{-1} were employed to evaluate the capacitance retention of the two SSCs, with the results shown in Fig. 6e–g. For the PVDF-SSC, a slight decrease in specific capacitance was observed as the bending angle increased, retaining 92.3% of its capacitance at 150°, but showing a significant drop to 71% at 180°. In contrast, the AFAO-SSC exhibited a slight increase in capacitance at a bending angle of 45° and subsequently maintained a stable capacitance retention of around 102%. This result may be attributed to the increased density of hydrogen bonding when the MXene surface was modified with the AFAO, which enhances the adhesion of AFAO-MXene to the PET substrate and improves resistance to bending, as illustrated in Fig. 6a. This strengthened interfacial interaction is also expected to contribute to enhanced adhesion and mechanical durability of the SSCs under numerous bending cycles in the subsequent test below.

To further assess the deformation resistance and adhesion on the substrate of the two inks, cyclic bending tests were conducted with a fixed bending angle of 180°, and the summary results are shown in Fig. 6h (check Fig. S7 for full CV scanning results). During the first 50 cycles, a decline in capacitance was observed in both devices, with the PVDF-SSC showing a more pronounced decrease, retaining only 83.1% of its initial value. After a brief performance plateau, the capacitance of the PVDF-SSC dropped significantly after 500 cycles, reaching only 21.5% retention. In contrast, the AFAO-SSC experienced only a slight decrease in capacitance during the first 50 cycles, followed by stable performance, maintaining 100% for 200 cycles before gradually increasing to over 211.9% after 1500 cycles. The increase in specific capacitance after mechanical deformation was previously reported, particularly in flexible supercapacitors employing 2D materials.[50–52] This enhancement in capacitance was previously observed in flexible supercapacitors employing 2D materials and is typically attributed to bending-induced expansion of interlayer spacing, which exposes more electroactive sites.[51,53] However, excessive bending may also create microcracks that disrupt connectivity and reduce structural integrity, ultimately increasing charge transfer resistance. The observed reduction in charge storage performance of the PVDF-SSC could be attributed to this phenomenon. Even though interlayer spacing between MXene sheets may also expand during bending to create additional charge storage space, the inherently bulky molecular structure of PVDF likely hinders electrolyte ions from accessing these expanded regions, as previously discussed. In contrast, the AFAO forms chemical bonds with the MXene surface that could improve interfacial contact after solvent removal without aggregation to each other and preserve electrode integrity under mechanical stress by preventing flake separation. This bonding enables efficient ion diffusion to an expanded zone easily—an advantage rarely achieved through physical interaction between MXene and a large molecule polymer.

To clarify the above observation and investigate the ion diffusion kinetics related to the charge storage behaviour, EIS of the AFAO-SSC and PVDF-SSC before and after bending was performed. The resulting Nyquist plots, along with their corresponding equivalent circuits, are shown in Fig. 6i. In the low-frequency region, the 45° linear part (Warburg impedance) is related to the ion diffusion resistance within porous electrode material, with a longer length corresponding to a larger ion transport resistance. Before and after bending, the AFAO-SSC exhibited behaviour resembling that of an ideal capacitor in the low-frequency region, as evidenced by the nearly vertical slopes. While the R_s value slightly increased in both SSCs, the R_{ct} of the AFAO-SSC decreased from 11.7 Ω to 3.35 Ω, indicating improved charge transfer. Meanwhile, the R_{ct} of the PVDF-SSC rose sharply from 25.13 Ω to 109.7 Ω. The Nyquist plot of the PVDF-SSC also exhibited a nearly horizontal slope in the low-frequency region—characteristic of Warburg impedance—indicating hindered ion diffusion. The Warburg coefficient (σ) of the PVDF-SSC increased significantly from 34.87 to 208.4 after 500 bending cycles, while only a negligible rise was observed in the AFAO-SSC (from 63.77 to 64.8) even after 1500 cycles. This sharp increase in σ for the PVDF-SSC corresponds to a sudden decline in charge storage performance in the 500th bending cycle, suggesting that ion diffusion was severely hindered due to microcrack formation or disruption of the internal conductive network, ultimately resulting in the near-complete loss of the capacitor's intrinsic charge storage behaviour. In contrast, the minimal change in σ for the AFAO-SSC indicates that ion transport pathways remained accessible, highlighting the role of the AFAO in enhancing mechanical resilience and preserving electrochemical performance under repeated deformation. These results confirm that mechanical deformation had disrupted the internal conductive network or generated microcracks in the PVDF-SSC, leading to poor ion accessibility and reduced charge storage capability, whereas AFAO modification not only enhances mechanical properties but also promotes efficient ion transport.

3. Experimental

3.1. Materials

Commercial Ti_3AlC_2 powders (99.8 wt% pure, Sigma-Aldrich), hydrochloric acid (HCl, 37%, Sigma-Aldrich), lithium fluoride (LiF, 99.98%, ThermoFisher), sulfuric acid (H_2SO_4, 98%, Sigma-Aldrich), polyvinylidene fluoride (PVDF, M_w = 534 000, Sigma-Aldrich), polyvinyl alcohol (PVA, M_w = 124 000, Sigma-Aldrich), dimethyl sulfoxide (DMSO, 99.8%, Samchun Pure Chemical Co.), isophorone diisocyanate (IPDI, Sigma-Aldrich), glycerol propoxylate (GP, M_w = 266 g mol^{-1}, KPX Chemical Co., Ltd), (3-

aminopropyl) triethoxysilane (APTES, Sigma-Aldrich), poly(ethylene glycol) (PEG, M_w = 300 g mol^{-1}, Sigma-Aldrich), dibutyltin dilaurate (DBTDL, Sigma-Aldrich), and acetone (Sigma-Aldrich).

3.2. Preparation of MXene colloidal solution

MXene nanosheets were synthesized through the following procedure. First, 1.6 g of LiF was dissolved in 20 mL of 9 M hydrochloric acid and stirred to form a homogeneous solution. Then, 1 g of Ti_3AlC_2 MXene powder was slowly added to the solution. The mixture was stirred at 45 °C for 24 h using a magnetic bar. After etching, the suspension was washed with deionized water by centrifugation at 3500 rpm until the pH exceeded 5, and the resulting slurry was collected as multilayered MXene sheets. The resulting MXene slurry was then mixed with deionized water and ultrasonicated for 30 minutes under a nitrogen atmosphere in the presence of ice packs. The mixture was subsequently centrifuged at 3500 rpm for 30 minutes, and the dark green supernatant, containing delaminated MXene flakes, was carefully decanted for use in the next step.

3.3. MXene surface modification with AFAO

The AFAO used to modify the surface of MXene nanosheets was synthesized using a three-step reaction procedure as described in our previous reports. The chemical structure of the resulting AFAO is shown in Fig. S1.[54–56]

The preparation procedure of AFAO-MXene is detailed as follows: the delaminated MXene solution collected from the previous step was subjected to solvent exchange with DMSO using centrifugation three times at 10 000 rpm for 15 minutes. After that, the AFAO was added to achieve a mass ratio of the AFAO to MXene of 1 : 10. The mixture was stirred at high speed for 6 hours before 2–3 drops of 0.1 M HCl were added as a catalyst. The resulting mixture was kept stirring with a magnetic bar for 48 hours at 60 °C to allow the hydrolysis and condensation reactions to proceed completely. Finally, the suspension was washed repeatedly with pure DMSO to remove the unreacted AFAO. The modified MXene in DMSO (hereafter referred to as AFAO-MXene) was redispersed by vortex mixing for 30 minutes, followed by 30 minutes of sonication to get homogeneous ink. The obtained MXene ink was subsequently used for flexible electrode fabrication.

3.4. Fabrication of flexible solid-state supercapacitors

3.4.1 Substrate pretreatment. The PET substrate was first subjected to a cleaning process using DI water and ethanol to eliminate contaminants.

3.4.2 Preparation of the gel electrolyte. Initially, 1 g of PVA was dissolved in 10 mL of deionized (DI) water and heated to 85 °C under continuous stirring for 3 hours until a clear, transparent gel was obtained. Subsequently, 1 g of concentrated H_2SO_4 was added to the resulting 10 wt% PVA gel, followed by stirring for an additional 30 minutes.

3.4.3 Fabrication of the flexible electrode. The fabrication of the flexible electrode was carried out as follows: 1 cm × 1 cm for three-electrode system testing and 1 cm × 2 cm for flexible all-solid-state supercapacitor assembly. The mass loading was maintained at 1 mg cm^{-2}. The AFAO–MXene mixture was drop-cast onto a PET substrate placed on a hot plate at 60 °C, followed by 24 hours of vacuum drying at 100 °C to completely remove residual DMSO. One end of the electrode was coated with silver paste and connected to copper tape, serving as the current collector. Both the pristine MXene electrode and the PVDF-MXene electrode were fabricated using the same procedure described above. In the case of the PVDF-MXene electrode, some of the total DMSO used for ink preparation was reserved for dissolving PVDF before mixing with the MXene solution, to achieve a mass ratio of PVDF to MXene of 1 : 10. However, for the pristine MXene electrode, only single-layer MXene flakes dispersed in DMSO were used. Pristine MXene was dispersed in DMSO and stirred for 2 hours, followed by drop-casting the dispersion onto a PET substrate with the same mass loading as the PVDF-MXene and AFAO-MXene electrodes, without the addition of any binder or conductive additive. The electrode was then dried and tested using CV, GCD, and EIS to determine the original specific capacitance and electrochemical characteristics. It is important to note that coating pristine MXene directly onto PET without a binder renders the electrode unsuitable for electrochemical testing under mechanical deformation or for fabricating solid-state devices.

3.4.4 Assembly of MXene-based SSCs. For the assembly of solid-state devices, the PVA/H_2SO_4 gel electrolyte was gently applied onto the active area of the electrodes. The electrodes were then dried overnight naturally at room temperature. Finally, two identical electrodes were aligned face-to-face and pressed together, forming a configuration where the solid electrolyte on each side acted as a thin interfacial separator. The SSC assembled from PVDF-MXene electrodes is referred to as the PVDF-SSC, while that based on AFAO-MXene electrodes is referred to as the AFAO-SSC.

3.4.5 Characterization of materials. High-resolution field-emission scanning electron microscopy (FE-SEM) was performed using a JSM-7800F microscope (JEOL, Japan). The X-ray photoelectron spectrometer (XPS) measurements were performed using the K Alpha+ system (Thermo Scientific, UK). XRD patterns were obtained with an AXS GmbH X-ray diffractometer (Bruker, Germany) using Cu Kα radiation (λ = 1.5406 Å) over the range of 2θ = 0–60.0°. The thin-film sheet resistance was tested with a Loresta GX MCP-T700 resistivity meter (Nittoseiko Analytech, Japan). The Fourier transform infrared (FT-IR) spectra were obtained using a Nicolet iS5 FT-IR spectrometer (Thermo Scientific, USA), equipped with an attenuated total reflection (ATR) setup. A thermogravimetric analyzer (TGA N-1000, Scinco, Korea) was used to analyze thermal properties of MXene under nitrogen.

3.4.6 Electrochemical measurements. Electrochemical characterization, including CV, GCD, and EIS, was carried out on an electrochemical workstation (SP-150e, EC-lab). Ag/AgCl in saturated 3 M KCl solution was selected as the reference electrode, and Pt was used as the counter electrode. All the scan rates of CV were tested from 5 mV s^{-1} to 150 mV s^{-1}, and current densities of GCD were from 1 to 10 A g^{-1}. The EIS was tested from the frequencies of 100 kHz to 100 mHz at the open

circuit potential. In addition, the cycling stability and bending stability of the flexible solid-state supercapacitors are also considered.

The specific capacitance was calculated from the CV curves and GCD profile according to the following equations:

$$C_s = \frac{A}{2 \times m \times K \times \Delta V} (\mathrm{F\ g^{-1}}) \quad (1)$$

$$C_s = \frac{I \times \Delta t}{m \times \Delta V_{\mathrm{eff}}} (\mathrm{F\ g^{-1}}) \quad (2)$$

$$\Delta V_{\mathrm{eff}} = \Delta V_{\mathrm{window}} - \Delta V_{\mathrm{IR}}$$

where C_s (F g^{-1}) is the specific capacitance; ΔV_{eff} (V) refers to the effective potential window after subtracting IR drop; m (g) refers to the active mass of the sample; A represents the area of the curve; K (mV s^{-1}) represents the scan rate; Δt (s) represents the discharging time.

4. Conclusions

In conclusion, this study introduces a new fabrication strategy employing an AFAO as a multifunctional binder for MXene ink, applied to flexible supercapacitor electrodes. The introduction of this multifunctional binder simultaneously enabled stable nanodispersion of MXene in organic solvents, enhanced interfacial adhesion to plastic substrates such as PET films, and retention of MXene's intrinsic electrochemical properties without the need for additional conductive additives. The flexible AFAO-MXene supercapacitor electrodes retained up to 94% of the original specific capacitance of pristine MXene, delivering a gravimetric capacitance of 211.2 F g^{-1} at 1 A g^{-1} in 1 M H_2SO_4 aqueous electrolyte. Notably, SSCs fabricated from AFAO-MXene ink exhibited superior specific capacitance and mechanical durability compared to PVDF-MXene, maintaining stable performance even after 1500 bending cycles. This surface modification strategy is expected to facilitate broader applications across various MXene materials, offering a simplified approach to ink formulation and device fabrication. This work lays a solid foundation for the practical implementation of MXene-based inks in next-generation flexible electronics and high-performance energy storage devices. It is expected that the capacitance can be further improved by optimizing other parameters. For future research along this direction or similar routes, the following aspects may need to be considered: MXene flake size, the mass ratio of MXene to the AFAO, adding a small amount of conductive fillers, using environmentally friendly solvents, and leveraging the steric stabilization of the AFAO in different solvents.

Author contributions

J. Y. K: supervision, conceptualization, methodology, writing – review & editing, resources, project administration, funding acquisition. T. T. D.: writing – original draft, review & editing, methodology, investigation, formal analysis, validation, conceptualization. S. H. K.: conceptualization, writing – review & editing, formal analysis. We used the AI chatbot (ChatGPT) only for grammar correction for this manuscript and guarantee that all intellectual content, data analysis, and scientific conclusions were the responsibility of the authors; there is no plagiarism in this paper, including in text and images produced using the AI.

Conflicts of interest

There are no conflicts to declare.

Data availability

Data that support the findings of this study are available from the corresponding author upon reasonable request. No software or code has been included.

The data supporting this article have been included as part of the Supplementary Information (SI). Supplementary information: chemical structure of the AFAO, SEM images of MAX phase Ti_3AlC_2 and multilayer $Ti_3C_2T_x$; zeta potential of pristine MXene and AFAO-MXene; cyclic voltammetry (CV) measurements of the pristine MXene electrode, PVDF-MXene electrode, AFAO-MXene electrode, and the AFAO-SSC at different voltage windows; charge–discharge profile for pristine-MXene, PVDF-MXene, and AFAO-MXene; CV scanning curves of the PVDF-SSC and AFAO-SSC at different scan rates; CV scanning curves of the PVDF-SSC and AFAO-SSC at various bending cycles at a 180° bending angle; summary of the XPS fit peak of O 1s of pristine MXene and AFAO-MXene; fitted equivalent circuit elements of pristine MXene, PVDF-MXene and AFAO-MXene electrodes; fitted equivalent circuit elements of the PVDF-SSC and AFAO-SSCf before and after bending at 180°. Video S1: AFAO-MXene ink in DMSO after 2 months of storage; Video S2: quick testing of the adhesion of AFAO-MXene ink on PET; Video S3: the bending test set-up for the symmetric supercapacitor. See DOI: https://doi.org/10.1039/d5ta06789h.

Acknowledgements

This work was supported by the Nano & Material Technology Development Program through the National Research Foundation of Korea (NRF), funded by the Ministry of Science and ICT (RS-2024-00444986), and by an NRF grant funded by the Korean government (RS-2025-16069685). We used AI chatbot (ChatGPT) only for grammar correction for this manuscript; guarantee all intellectual content, data analysis, and scientific conclusions were the responsibility of the authors; there is no plagiarism in this paper, including in text and images produced by the AI.

References

1 B. Anasori, Y. Xie, M. Beidaghi, J. Lu, B. C. Hosler, L. Hultman, P. R. C. Kent, Y. Gogotsi and M. W. Barsoum, *ACS Nano*, 2015, **9**, 9507–9516.

2 M. Naguib, M. Kurtoglu, V. Presser, J. Lu, J. Niu, M. Heon, L. Hultman, Y. Gogotsi and M. W. Barsoum, *Adv. Mater.*, 2011, **23**, 4248–4253.
3 V. M. Hong Ng, H. Huang, K. Zhou, P. S. Lee, W. Que, J. Z. Xu and L. B. Kong, *J. Mater. Chem. A*, 2017, **5**, 3039–3068.
4 J. Zhang, N. Kong, S. Uzun, A. Levitt, S. Seyedin, P. A. Lynch, S. Qin, M. Han, W. Yang, J. Liu, X. Wang, Y. Gogotsi and J. M. Razal, *Adv. Mater.*, 2020, **32**(23), DOI: 10.1002/adma.202001093.
5 R. Ma, Z. Chen, D. Zhao, X. Zhang, J. Zhuo, Y. Yin, X. Wang, G. Yang and F. Yi, *J. Mater. Chem. A*, 2021, **9**, 11501–11529.
6 T. P. Nguyen, D. M. Tuan Nguyen, D. L. Tran, H. K. Le, D.-V. N. Vo, S. S. Lam, R. S. Varma, M. Shokouhimehr, C. C. Nguyen and Q. Van Le, *Mol. Catal.*, 2020, **486**, 110850.
7 B. Ratzker, O. Messer, B. Favelukis, S. Kalabukhov, N. Maman, V. Ezersky and M. Sokol, *ACS Nano*, 2023, **17**, 157–167.
8 M. Mahato, S. Nam, G. Valurouthu, H. Yoo, M. Garai, J.-S. Kim, W. Oh, J. Ha, V. Kumar, C. W. Ahn, Y. Gogotsi and I.-K. Oh, *ACS Nano*, 2025, **19**(28), 25757–25769.
9 N. My Tran, Q. Thanh Hoai Ta, A. Sreedhar and J.-S. Noh, *Appl. Surf. Sci.*, 2021, **537**, 148006.
10 W. Luo, Y. Sun, Y. Han, J. Ding, T. Li, C. Hou and Y. Ma, *Electrochim. Acta*, 2023, **441**, 141818.
11 J. Zhang, D. Jiang, L. Liao, L. Cui, R. Zheng and J. Liu, *Chem. Eng. J.*, 2022, **429**, 132232.
12 N. Chen, Y. Zhou, S. Zhang, H. Huang, C. (John) Zhang, X. Zheng, X. Chu, H. Zhang, W. Yang and J. Chen, *Nano Energy*, 2021, **85**, 106007.
13 H. Huang, J. He, Z. Wang, H. Zhang, L. Jin, N. Chen, Y. Xie, X. Chu, B. Gu, W. Deng and W. Yang, *Nano Energy*, 2020, **69**, 104431.
14 T. Liu, L. Finn, M. Yu, H. Wang, T. Zhai, X. Lu, Y. Tong and Y. Li, *Nano Lett.*, 2014, **14**, 2522–2527.
15 J. Wang, Y. Huang, S. Zhang, X. Du, Z. Duan and X. Sun, *J. Mater. Sci. Technol.*, 2023, **147**, 112–123.
16 Q. Meng, K. Cai, Y. Chen and L. Chen, *Nano Energy*, 2017, **36**, 268–285.
17 H. Xu, L. Cui, Z. Lei, M. Xu and X. Jin, *Electrochim. Acta*, 2022, **436**, 141408.
18 M. Boota, M. P. Paranthaman, A. K. Naskar, Y. Li, K. Akato and Y. Gogotsi, *ChemSusChem*, 2015, **8**, 3576–3581.
19 L. Yu, L. Hu, B. Anasori, Y.-T. Liu, Q. Zhu, P. Zhang, Y. Gogotsi and B. Xu, *ACS Energy Lett.*, 2018, **3**, 1597–1603.
20 R. Dominko, M. Gaberšček, J. Drofenik, M. Bele and J. Jamnik, *Electrochim. Acta*, 2003, **48**, 3709–3716.
21 D. Zhang, J. Cao, X. Zhang, N. Insin, R. Liu and J. Qin, *ACS Appl. Energy Mater.*, 2020, **3**, 5949–5964.
22 Z. Fan, Y. Wang, Z. Xie, D. Wang, Y. Yuan, H. Kang, B. Su, Z. Cheng and Y. Liu, *Advanced Science*, 2018, **5**(10), DOI: 10.1002/advs.201800750.
23 Q. Fu, X. Wang, N. Zhang, J. Wen, L. Li, H. Gao and X. Zhang, *J. Colloid Interface Sci.*, 2018, **511**, 128–134.
24 N. Lingappan, L. Kong and M. Pecht, *Renewable Sustainable Energy Rev.*, 2021, **147**, 111227.
25 J.-K. Yoo, Y. Oh, T. Park, K. E. Lee, M.-K. Um and J.-W. Yi, *Energy Technol.*, 2019, **7**(5), DOI: 10.1002/ente.201800845.
26 H. N. Le, C. Lee, W. Jung and J. Kim, *Coatings*, 2023, **13**, 1997.
27 T. T. Duong, M. Linh Le and J. Kim, *Mater. Today Commun.*, 2024, **41**, 110453.
28 L. Verger, V. Natu, M. Carey and M. W. Barsoum, *Trends Chem.*, 2019, **1**, 656–669.
29 W. Sun, S. A. Shah, Y. Chen, Z. Tan, H. Gao, T. Habib, M. Radovic and M. J. Green, *J. Mater. Chem. A*, 2017, **5**, 21663–21668.
30 Y. Li, X. Zhou, J. Wang, Q. Deng, M. Li, S. Du, Y.-H. Han, J. Lee and Q. Huang, *RSC Adv.*, 2017, **7**, 24698–24708.
31 S.-B. Ko, Y. Sun, G. Park, H. J. Choi, J. G. Kim, J. B. Kim, H. J. Jung, G. S. Lee, S. Hong, S. Padmajan Sasikala and S. O. Kim, *ACS Appl. Mater. Interfaces*, 2023, **15**, 32707–32716.
32 T. Parker, D. Zhang, D. Bugallo, K. Shevchuk, M. Downes, G. Valurouthu, A. Inman, B. Chacon, T. Zhang, C. E. Shuck, Y.-J. Hu and Y. Gogotsi, *Chem. Mater.*, 2024, **36**, 8437–8446.
33 Y. Wei, W. Luo, Z. Zhuang, B. Dai, J. Ding, T. Li, M. Ma, X. Yin and Y. Ma, *Adv. Compos. Hybrid Mater.*, 2021, **4**, 1082–1091.
34 Y. Li, B. Xin, Z. Lu, X. Zhou, Y. Liu and Y. Hu, *Int. J. Energy Res.*, 2021, **45**, 9229–9240.
35 Z. Bao, C. Lu, X. Cao, P. Zhang, L. Yang, H. Zhang, D. Sha, W. He, W. Zhang, L. Pan and Z. Sun, *Chin. Chem. Lett.*, 2021, **32**, 2648–2658.
36 Y. Gong, P. Xue, X. Wang, S. Ma and X. Xu, *J. Mater. Sci.*, 2024, **59**, 12447–12463.
37 G. Xie, L. Wang, Q. Zhu, L. Xu, K. Song and Z. Yu, *ACS Appl. Nano Mater.*, 2022, **5**, 9678–9687.
38 Y. Liu, Z. Xu, X. Ji, X. Xu, F. Chen, X. Pan, Z. Fu, Y. Chen, Z. Zhang, H. Liu, B. Cheng and J. Liang, *Nat. Commun.*, 2024, **15**, 5354.
39 A. Mirabedini, S. M. Mirabedini, A. A. Babalou and S. Pazokifard, *Prog. Org. Coat.*, 2011, **72**, 453–460.
40 M. Mokhtarimehr, M. Pakshir, A. Eshaghi and M. H. Shariat, *Thin Solid Films*, 2013, **532**, 123–126.
41 L. Ning, J. Chen, J. Sun, Y. Liu, D. Yi and J. Cao, *ACS Omega*, 2021, **6**, 23683–23690.
42 F. Zhang, W. Liu, S. Wang, C. Liu, H. Shi, L. Liang and K. Pi, *Composites, Part B*, 2021, **217**, 108900.
43 J. Li, X. Yuan, C. Lin, Y. Yang, L. Xu, X. Du, J. Xie, J. Lin and J. Sun, *Adv. Energy Mater.*, 2017, **7**(15), DOI: 10.1002/aenm.201602725.
44 A. Numan, S. Rafique, M. Khalid, H. A. Zaharin, A. Radwan, N. A. Mokri, O. P. Ching and R. Walvekar, *Mater. Chem. Phys.*, 2022, **288**, 126429.
45 Y. Liu, Y. Zhu, Z. Xu, X. Xu, P. Xue, H. Jiang, Z. Zhang, M. Gao, H. Liu and B. Cheng, *Carbohydr. Polym.*, 2024, **327**, 121674.
46 A. Sengupta, B. V. B. Rao, N. Sharma, S. Parmar, V. Chavan, S. K. Singh, S. Kale and S. Ogale, *Nanoscale*, 2020, **12**, 8466–8476.
47 V. Natu, M. Benchakar, C. Canaff, A. Habrioux, S. Célérier and M. W. Barsoum, *Matter*, 2021, **4**, 1224–1251.
48 M. Han, X. Yin, H. Wu, Z. Hou, C. Song, X. Li, L. Zhang and L. Cheng, *ACS Appl. Mater. Interfaces*, 2016, **8**, 21011–21019.

49 X. Wang, X. Shen, Y. Gao, Z. Wang, R. Yu and L. Chen, *J. Am. Chem. Soc.*, 2015, **137**, 2715–2721.
50 E. Kim, J. Song, T.-E. Song, H. Kim, Y.-J. Kim, Y.-W. Oh, S. Jung, I.-S. Kang, Y. Gogotsi, H. Han, C. W. Ahn and Y. Lee, *Chem. Eng. J.*, 2022, **450**, 138456.
51 C. (John) Zhang, B. Anasori, A. Seral-Ascaso, S. Park, N. McEvoy, A. Shmeliov, G. S. Duesberg, J. N. Coleman, Y. Gogotsi and V. Nicolosi, *Adv. Mater.*, 2017, **29**(36), DOI: 10.1002/adma.201702678.
52 Q. Liang, T. Jiang, S. Zhang, X. Long, S. Yan, R. Dong, T. Luo, X. Xu and F. Wang, *J. Energy Storage*, 2021, **41**, 102858.
53 C. (John) Zhang, T. M. Higgins, S.-H. Park, S. E. O'Brien, D. Long, J. N. Coleman and V. Nicolosi, *Nano Energy*, 2016, **28**, 495–505.
54 T. T. Duong, M. Linh Le and J. Kim, *Mater. Today Commun.*, 2024, **41**, 110453.
55 S. Cho, N. Kim, S. Lee, H. Lee, S.-H. Lee, J. Kim and J.-W. Choi, *Chemosphere*, 2016, **156**, 302–311.
56 M. L. Le, M. C. Jung, H. W. Kim and J. Kim, *Compos. Interfaces*, 2022, **29**, 1619–1635.